Improving TiO_2 Anatase Nanostability via Interface Segregation: The Role of the Ionic Radius

Andre L. da Silva[a], * Jefferson Bettini[b], Andre A. Bernardes[a], Ricardo H. R. Castro[c], and Douglas Gouvêa[a]

[a] *Department of Metallurgical and Materials Engineering, Polytechnic School - University of São Paulo, São Paulo 05508-030, Brazil;*

[b] *Brazilian Nanotechnology National Laboratory (LNNano), Rua Giuseppe Maximo Scolfaro 10000, BR-13083100 Campinas, SP, Brazil;*

[c] *Department of Materials Science and Engineering, University of California, Davis, One Shields Avenue, Davis, CA 95616, United States;*

* E-mail: andresilva.urussanga@gmail.com. Tel. +55 (11) 97414-5238.

Abstract

Titanium dioxide nanoparticles are of particular interest in photocatalysis and artificial photosynthesis studies. Their properties are dependent on parameters such as the crystal polymorph, *e.g.*, anatase/rutile phases, the specific surface area, and the capacity to adsorb CO_2 and H_2O gas molecules. A cause-effect relationship exists between those parameters, the surface thermochemistry, and the performance in application. However, the lack of systematic thermodynamic data has hindered a more comprehensive understanding to enable control. This work investigates the relationship between the surface thermochemistry of alkaline earth doped TiO_2 and the associated micro and nanostructural features. TiO_2 nanoparticles doped with Mg^{2+}, Ca^{2+}, Sr^{2+}, or Ba^{2+} showed spontaneous segregation of dopants to the nanoparticles' interfaces, leading to incremental surface energy reduction as directly measured by microcalorimetry of adsorption. The phenomenon was a direct function of ionic radius and led to the improved thermal stability of the nanoparticles against coarsening, stabilizing the anatase polymorph and increasing the specific surface area.

Introduction

Titanium dioxide (TiO_2) is used in various applications, ranging from everyday products, such as sunscreens, food coloring, and paints, to advanced devices like photovoltaic cells. TiO_2 nanoparticles, in particular, have been successfully tested in a series of environmental and biomedical applications, such as photocatalytic (PC) degradation of pollutants, water purification, artificial photosynthesis (AP), biosensing, and drug delivery.[1] The interest in TiO_2 is mainly driven by its relatively low cost, high chemical stability, low toxicity, and high PC activity,[2] which contributed to spreading its use beyond academic studies.

Three polymorphs of TiO_2 occur at atmospheric pressure: brookite, anatase, and rutile, the last two being the most common.[3] Although rutile is the thermodynamically stable state of TiO_2, the anatase commonly exists at the nanoscale.[4,5] This is associated with the increased contribution of surface energies to the system's total energy at reduced dimensions. The raised surface areas lead to a crossover in the thermodynamic stability of the two polymorphs at a critical small particle size. That implies anatase has a range of particle sizes in which it is (meta)stable, as long as coarsening is avoided. However, during synthesis or application, coarsening may occur, and anatase particles transform irreversibly to rutile. This transformation (ART - anatase to rutile transition) limits the operation and processing temperatures of the active anatase phase, affecting applications in gas sensors, porous gas separation membranes,[3] and self-cleaning ceramic tiles.[6,7]

One of the possible strategies to postpone ART and improve the nano-stability of TiO_2 particles is the usage of segregated dopants on the surface.[7,6,8,9] The phenomenon leads to ART suppression.[8] Still, since segregated ions generally substitute Ti^{4+} on the surface, dopants simultaneously change the physical chemistry of the surface and affect aspects such as PC performance.[6,8] While surface segregation can serve as an effective surface designing tool, further studies are still necessary to understand the complex interdependencies between segregation, the physical chemistry of the surface, its thermodynamics, and the related micro/nanostructural evolutions.

In crystalline systems, four kinds of driving forces govern surface segregation. The driving force for the phenomenon depends on the difference in surface energy between the dopant and the host (ΔH_σ), the elastic solute strain energy due to the size difference between the dopant and host ions (ΔH_ε), the solute-solvent interaction (ΔH_ω),

and the electrostatic potential/charge compensation (ΔH_ϕ). Thus, this so-called enthalpy of segregation (ΔH_{seg}) becomes:[10,11]

$$\Delta H_{seg} = \Delta H_\sigma + \Delta H_\varepsilon + \Delta H_\omega + \Delta H_\phi \quad (1)$$

While eq. 1 informs dopant selection, because of some simplifications of the formalism, predictions are still unreliable and need experimental benchmarks.

To advance the dopant segregation theory, we selected a series of alkaline earth ions as dopants for TiO_2. The ions show the same charge (2+) but distinct ionic radius (86, 114, 132, and 149 pm, for Mg^{2+}, Ca^{2+}, Sr^{2+}, and Ba^{2+}, respectively). The effect of the ionic radius mismatch between the solute and the solvent on the segregation behavior is associated with the elastic solute strain energy (ΔH_ε), eq. 2.[10]

$$\Delta H_\varepsilon = \frac{24\pi \mathrm{K G r_1 r_2 (r_1 r_2)^2}}{4\mathrm{G r_1} + 3\mathrm{K r_2}} \quad (2)$$

here, r_1 and r_2 are the ionic radius of the solute and the solvent ions, respectively, G is the stiffness modulus, and K is the compression modulus.

The equation indicates that higher mismatches increase the potential for segregation. The present work aims to study this trend by exploring alkaline earth ions in TiO_2. These ions are particularly interesting as dopants for TiO_2 because they can increase the alkalinity of the surface and favor H_2O adsorption for AP.[12] We will quantify the segregation of the ions to the surface and grain boundary regions using surface lixiviation and correlate the data with the microstructural evolution and the interfacial energies. The goal is to unravel the interdependence between nano-grain stability and surface energy decrease as a function of the dopant ionic radius in TiO_2.

Experimental Methods

Synthesis of Undoped and Doped TiO_2 Nanoparticles.

TiO_2-based powders containing MgO, CaO, SrO, or BaO were synthesized by the polymeric precursor method. The titanium-oxide polymeric precursor was prepared by mixing 19.4 wt % titanium (IV) isopropoxide (Sigma-Aldrich, ≥ 97.00 wt.% purity) with 45.4 wt % ethylene glycol (Synth, $C_2H_6O_2$, ≥ 99.00 wt.% purity) at 40 °C, followed by heating to 70 °C and addition of 35.2 wt % anhydride citric acid (Synth,

$C_6H_8O_7$, ≥ 99.00 wt.% purity). Thus, the solution was heated to 120 °C for polyesterification. The addition of MgO, CaO, SrO, or BaO was made using acid solutions (0.2 mol/L) of each dopant. These solutions were obtained by solubilizing the appropriate amount of $Mg(NO_3)_2$, $Ca(NO_3)_2$, $Sr(NO_3)_2$, or $Ba(NO_3)_2$ in an aqueous nitric acid solution (0.1 M), followed by chemical analysis.

The samples were prepared by mixing calculated amounts of the solutions and the precursor with the target molar dopant concentrations of 0.0, 0.1, 1.0 and 5.0 %. The samples were labeled in this paper as listed in Table 1. The calcination was performed in two steps: first, each sample was held at 350 °C for 4 h to decompose the organic trace. Thus, the powders were manually ground with a mortar and pestle and treated in the air at 350 °C for 15 h to complete the oxidation and particle crystallization.

Table 1. Samples label according to the dopant molar concentration.

Mol% of the dopant	MgO-doped TiO_2	CaO-doped TiO_2	SrO-doped TiO_2	BaO-doped TiO_2
0.0	TiO_2	TiO_2	TiO_2	TiO_2
0.1	Ti001Mg	Ti001Ca	Ti001Sr	Ti001Ba
1.0	Ti010Mg	Ti010Ca	Ti010Sr	Ti010Ba
5.0	Ti050Mg	Ti050Ca	Ti050Sr	Ti050Ba

Sample Characterization.

X-ray diffraction patterns were collected using a Philips X'Pert PRO PW 3040/00 diffractometer with Cu Kα radiation at 0.02° steps per second over the 2θ range of 5-90 °. The lattice parameters were calculated using the X'Pert Highscore software. Crystallite sizes were calculated using whole profile fitting using Materials Studio 6.0 software with CaF_2 and anatase structures as standards. The chemical compositions were analyzed by inductively coupled plasma atomic emission optical spectroscopy (ICP OES) using a Spectro Across spectrometer. The samples were prepared by melting the powders with sodium borate, followed by acid digestion. The specific density of the powders was obtained using a Micrometrics AccuPyc II 1340 gas pycnometer after 200 purges for degassing. Specific surface area measurements were carried out using the Brunauer, Emmett, and Teller (BET) method with nitrogen gas adsorption (at 77 K) (Micromeritics Gemini VII). The samples were degassed at 300 °C for ~16 h using a Micromeritics VacPrep 061 before nitrogen adsorption.

Surface Segregation.

The surface excess of the dopants on TiO_2 nanoparticles was determined by (1) selective superficial lixiviation, (2) electron energy loss spectroscopy (EELS) in scanning electron transmission microscopy mode (STEM), (3) energy dispersive spectroscopy (EDS), and (4) X-ray photoelectron spectroscopy (XPS). The selective superficial lixiviation was performed by ultrasonication of ~100 mg of powder with 2 g of 0.1 M HNO_3 solution (pH = 1) for 1 h. Then, the samples were centrifuged at 13,000 rpm (10,390*g*) for 20 min. Approximately 1 g of the supernatant solution was collected, diluted in ~10 g of H_2O, and analyzed by inductively coupled plasma atomic emission optical spectroscopy (ICP OES) using a Spectro Across spectrometer.[13,11,14] The complete description of the selective superficial lixiviation method is shown in the supporting information file. Composition maps based on EELS and EDS measurements were performed exclusively in samples containing 5.0 mol% dopant: Ti050Mg (EDS), Ti050Sr (EELS), and Ti050Ba (EELS). Sample coarsening allowed particle sizes larger than the testing probes themselves, enabling better visualization of segregation. Ti050Mg, Ti050Sr and Ti050Ba were calcined at 500, 600, and 700 °C for 4 h, respectively. EELS was performed in the JEM-2100F (JEOL) equipped with an 863 GIF Tridiem spectrometer (Gatan). All measurements were carried out in scanning transmission electron microscopy (STEM) mode. The probe size was 0.7 nm, the pixel size for the EELS image spectrum was 0.5 nm, and the pixel time acquisition was 2 s for the line profile measurement. The probe size used for the EELS mapping was 1 nm, with a pixel size of 0.62 nm, and a pixel time acquisition of 0.2 s. The EDS measurement was also conducted in a JEM-2100F (JEOL) equipped with an SSD 80 mm^2 detector (Oxford). The measurement was carried out in STEM mode. The probe size used was 0.7 nm, the pixel size for EDS image spectrum was 0.475 nm, and the total pixel time acquisition was 0.3 s. The X-ray photoelectron spectroscopy (XPS) measurements were carried out using a ScientaOmicron ESCA+ spectrometer equipped with a monochromatic X-ray source (Kα 1486.6 eV) and a hemispherical type electron analyzer. During the measurements, the pressure in the analysis camera was 2×10^{-9} mbar. The survey and selected element spectra were registered at 0.1 and 0.5 eV energy steps, respectively. The composition was determined by the relative peak areas corrected by Scofield's atomic sensitivity factors with ~5 % precision. The spectra were deconvoluted using Voigt profiles with combinations of Gaussian (70 %) and

Lorentzian (30 %) terms. The width at half height varied between 1.2 and 2.0 eV, and the peak positions were determined with ~0.1 eV accuracy.

Surface Energy.

Water adsorption microcalorimetry was used to determine the surface energy of undoped and doped TiO_2. The instrument and methodology are detailed elsewhere.[15,16] In a typical experiment, 15−30 mg of powder, providing a total surface area of ~2 m^2, was placed into one side of a two-arm fork tube within the Setaram SetSYS Evolution Calvet microcalorimeter chamber calibrated against the enthalpy of gallium fusion. The empty arm was a reference while the microcalorimeter recorded the differential heat effects. The fork tube was connected to a 3Flex sorption analyzer (Micromeritics) to dose water vapor. The combined instruments measured the heat of water adsorption and the water coverage. The heat of adsorption is measured to an accuracy of ± 1% in each dosage. The samples were degassed at 200 °C for 12 h under vacuum to remove adsorbed water molecules before water adsorption. Degassing conditions were established by using thermogravimetry. During the experiment, the chamber was kept at 25 °C, and the dosing routine was programmed to be ~2 μmol H_2O per dose and equilibration time ~1.75 h for the first four doses, ~1 h for the fifth dose, ~0.75 h for sixth and seventh, and ~0.5 h from the eighth dose on. The equilibrium times were selected to be long enough for the calorimeter heat signal to return to the baseline.

The surface energies of the anhydrous samples were calculated using the Castro and Quach's derivation.[16] The method is based on a thermodynamic correlation between the heat of water adsorption on the surface and the surface energy itself. The interaction of water molecules with the surface of the nanopowders continuously affects the heat of water adsorption and the net surface energy. The adsorption reaction is highly energetic at low coverage and systematically decreases until it finds an energy plateau when the surface assumes a liquid-like state. Beyond this coverage, the heat of water adsorption remains constant at -44 kJ/mol (enthalpy of water condensation), and the net surface energy of the adsorbed water on nanoparticles becomes 0.072 J/m^2, which is that of liquid water. The surface energy of the anhydrous state can then be calculated based on eq. 3.

$$\gamma^s = \gamma_0^s + \theta \cdot \Delta H_{ads} \quad (3)$$

where θ is the surface coverage, ΔH_{ads} is the heat of water adsorption, γ_0^s is the surface energy of the anhydrous surface, and γ^s is the surface energy at the θ coverage. If ΔH_{ads} and the given coverage are identified at the water-like state, the surface energy is known as 0.072 J/m², and hence the anhydrous surface energy (at zero water coverage) can be computed.

Results and Discussion

Characterization of the nanoparticles.

The chemical compositions and density of the synthesized doped and undoped TiO_2 powders are shown in Table 2. The amount of dopant in TiO_2 nanoparticles was analyzed by ICP, and most samples were close to the nominal composition, being Ti050Sr the most divergent. Throughout the paper, we used the experimental chemical composition rather than the aimed compositions for clarity in graphing and calculations. For all compositions, the density decreased as the dopant concentration increased, except for SrO-doped TiO_2, which showed an abnormal behavior for 1 mol%. Density reduction with increasing dopant content could be expected when doping with MgO and CaO since the respective oxides have theoretical densities lower than TiO_2 (3.6 g/cm³ for MgO and 3.34 g/cm³ for CaO). However, by doping TiO_2 with BaO (and SrO), if a simple mixing rule is considered, an increase in density should be expected since the respective dopant oxides have relatively higher theoretical densities (4.7 g/cm³ for SrO and 5.72 g/cm² for BaO). The systematic decrease could be explained by the dopants being located on the surface of the nanoparticles rather than forming solid solutions or by the defect chemistry since the divalent dopants cause the formation of oxygen vacancies to maintain neutrality.

Table 2. Chemical analysis and density of all compositions.

	Target composition	MgO-doped TiO_2	CaO-doped TiO_2	SrO-doped TiO_2	BaO-doped TiO_2
Chemical analysis (x mol%)	0.00	0.00	0.00	0.00	0.00
	0.10	0.10	0.11	0.12	0.11
	1.00	0.73	0.85	1.05	1.01
	5.00	5.23	5.30	6.46	5.11
Density (g/cm³)	0.00	3.62 ± 0.01	3.62 ± 0.01	3.62 ± 0.01	3.62 ± 0.01
	0.10	3.47 ± 0.01	3.49 ± 0.01	3.46 ± 0.01	3.47 ± 0.01
	1.00	3.36 ± 0.01	3.35 ± 0.01	3.57 ± 0.01	3.32 ± 0.01

	5.00	3.33 ± 0.01	3.22 ± 0.01	3.04 ± 0.01	3.25 ± 0.01

The X-ray diffraction (XRD) patterns for undoped TiO_2 and doped with MgO, CaO, SrO, and BaO at different concentrations are shown in Figure 1. Anatase (JCPDS card no.71-1167) was the only phase found for all compositions, and the purity of the samples was confirmed by Rietveld analysis using the X'Pert Highscore software. Respective Miller indices are indicated in Figures 1a,b, and c. All samples showed relatively broad reflection peaks, typical of nanosized crystallites.

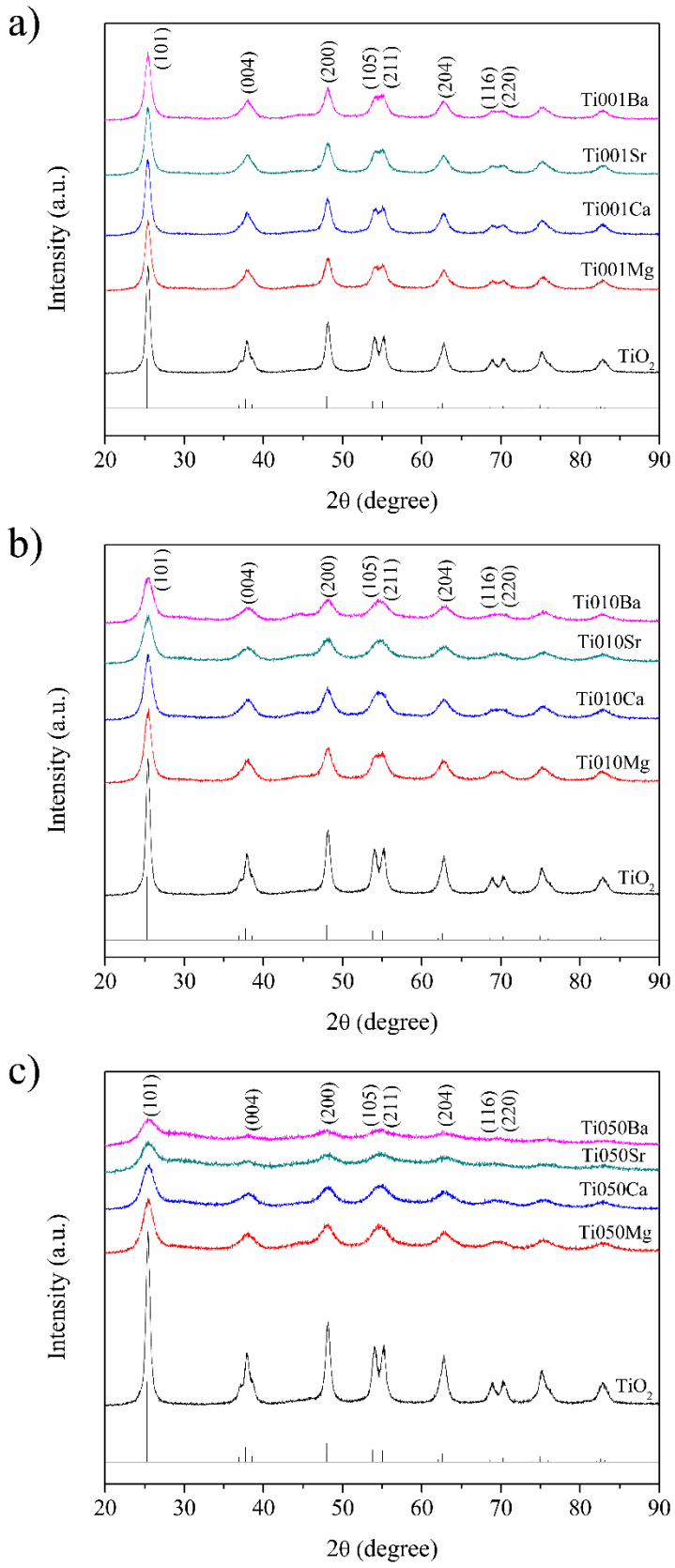

Figure 1. X-ray diffraction patterns of undoped TiO_2 and doped with MgO, CaO, SrO, and BaO at different concentrations. a) 0.1 mol%. b) 1.0 mol%. c) 5.0 mol%. The simulated XRD patterns of the

anatase phase are shown in the graph right below undoped TiO_2 patterns and the simulated structure is shown in Figure S1.

Figure 2a shows the results of the computed crystallite sizes. All tested ions decreased TiO_2 crystallite sizes. There is a slight difference, with crystallite sizes varying in the following order: MgO > CaO > SrO > BaO, i.e., the crystallite size scales inversely with the dopant ionic radius. Reduction in the crystallite size as a function of dopant content indicates increased nanostability against coarsening. According to general coarsening models,[17] the particle size is directly proportional to the surface energy, which depends on the surface segregation following the Gibbs adsorption isotherm model, and the diffusion. Provided that all dopants have similar charges, the diffusion coefficient should be affected equally in all instances, not playing a critical role in differentiating coarsening trends. On the other hand, an increase in surface excess shall cause surface energy reduction and, consequently, smaller crystallite sizes at a given temperature, as reported previously for different oxides.[13,18,11] To double check the crystallite sizes calculated using the XRD data, we have chosen two samples and performed TEM, which were Ti050Mg and Ti050Ba (doped samples with the smaller and higher ionic radius). The results are shown in Figures S2 and S3. Ti050Mg presented a crystallite domain size average equal to 6.4 ± 1.5 nm, while the values for the Ti050Ba sample were 4.9 ± 1.4 nm. These values agree with the crystallite sizes calculated by the XRD.

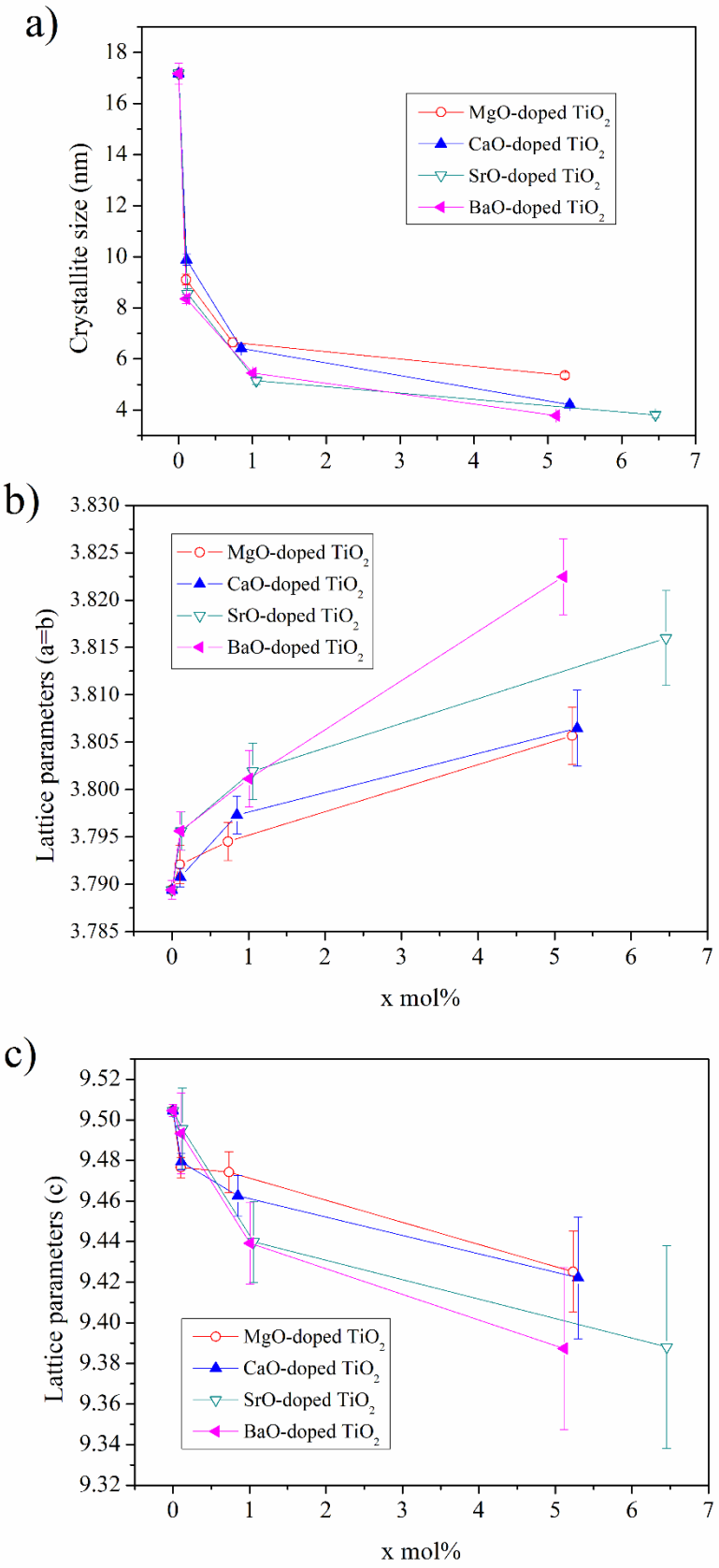

Figure 2. Average crystallite sizes and lattice parameters a=b and c of undoped TiO_2 and doped with MgO, CaO, SrO, and BaO at different concentrations (0.0 – 5.0 mol%).

The lattice parameters for all compositions are shown in Figures 2b,c. An expansion (i.e., positive strain) in lattice parameters *a* and *b* occurs while lattice *c* shrinks (i.e., negative strain) for all dopants, with BaO causing the most pronounced case. Since all dopants are divalent, the defect chemistry is not deemed responsible for the variations in the lattice volume between the chemistries. Changes in lattice parameters in small nanoparticles relate to the internal structure, which experiences high pressure due to the surface stress.[19] Many factors affect the surface stress of nanoparticles, including crystal structure, particle morphology and size, nanoparticle surface state, and surface environment, e.g., surface coating by organic molecules and adsorption of water molecules.[19] It is observed in Figures 2b,c that the lattice parameters are more affected when TiO_2 contains cations with higher ionic radius, which could be a consequence of the surface segregation.[11,20] We speculate dopants with higher ionic radius segregate to the topmost layer of the nanoparticle, increasing surface stress and, consequently, distorting the lattice parameters. In truth, variance in lattice parameters has also been associated with crystallite sizes. Both lattice expansion[21,22] and lattice contraction[13,23,24] may occur when crystallite sizes decrease. This effect is related to the synthesis and type of precursor, which can lead to surface-associated impurities.[19] The observed lattice distortions may have dual contributions from the crystallite sizes and surface stress.

Table 3. Specific surface area, total specific area, specific grain boundary area, and SGB/SSA ratio of all compositions.

	Target composition	MgO-doped TiO_2	CaO-doped TiO_2	SrO-doped TiO_2	BaO-doped TiO_2
Specific surface area (m^2/g)	0.00	45.3 ± 0.2	45.3 ± 0.2	45.3 ± 0.2	45.3 ± 0.2
	0.10	66.6 ± 0.3	65.7 ± 0.3	78.2 ± 0.4	77.2 ± 0.4
	1.00	76.7 ± 0.4	94.7 ± 0.5	110.0 ± 0.6	99.3 ± 0.5
	5.00	103.9 ± 0.5	117.6 ± 0.6	121.9 ± 0.6	109.8 ± 0.5
Total specific area (m^2/g)	0.00	114.2 ± 2.8	114.2 ± 2.8	114.2 ± 2.8	114.2 ± 2.8
	0.10	224.6 ± 5.0	205.8 ± 4.8	240.0 ± 5.0	244.8 ± 5.1
	1.00	317.7 ± 8.1	329.9 ± 6.4	386.0 ± 11.4	392.4 ± 7.9
	5.00	397.6 ± 8.3	523.0 ± 8.8	611.5 ± 17.7	576.5 ± 9.0
Specific grain boundary area (m^2/g)	0.00	34.46 ± 1.0	34.46 ± 1.0	34.46 ± 1.0	34.46 ± 1.0
	0.10	79.01 ± 2.1	70.03 ± 2.0	80.89 ± 2.1	83.79 ± 2.2
	1.00	120.51 ± 3.7	117.60 ± 2.9	137.98 ± 4.8	146.54 ± 3.7
	5.00	146.86 ± 3.8	202.68 ± 4.4	244.81 ± 8.3	233.32 ± 4.8
SGB/SSA ratio	0.00	0.76	0.76	0.76	0.76
	0.10	1.19	1.07	1.03	1.08
	1.00	1.57	1.24	1.25	1.48
	5.00	1.41	1.72	2.01	2.12

Table 3 lists the specific surface area (SSA) of all compositions calcined at 350 °C for 15 h. The evolution of the SSA followed the inverse trend from that observed for crystallite sizes (Figure 2a). The effect is consistent with the expectation that smaller particles have a larger specific surface area. However, the measured surface areas are relatively low, considering the crystallite sizes of the sample. That suggests the presence of agglomerates, with TiO_2 nanocrystals forming solid-solid interfaces not accessible by N_2 during the adsorption experiment. One can estimate the solid-solid interface area by calculating the hypothetical total specific surface area (TSA). Assuming nanocrystals are isolated and have a tetrakaidekahedral shape, one can write:

$$TSA = \frac{7.1}{\rho D} \tag{4}$$

where D is the average crystallite size, ρ is the powder density, and 7.1 is the shape factor. The TSA values for the TiO_2 nanocrystals are listed in Table 2. If TSA is a measure of all interfaces present in a particulate system, including solid-vapor interfaces and solid-solid formed by aggregation and sintering, the grain boundary area can be calculated as half of the difference between TSA and SSA:

$$SGB = (TSA - SSA)/2 \tag{5}$$

The specific grain boundary area (SGB) and the SGB/SSA ratio for the TiO_2 nanocrystals are listed in Table 3. The SGB increases as the dopant percentage increases at all compositions. We also observe SGB scales with the ionic radius of the dopant, similarly to the SGB/SSA ratio trend. This increase in TSA, SGB, and SGB/SSA ratio indicates a modification in the relative stability of interfaces, possibly because of the change in the balance of the interfacial energies due to dopant segregation. During coarsening, interfacial energies are the driving forces for coalescence, sintering, particle aggregation, and grain growth. These processes will take place in the direction of the greatest energy reduction. Higher values of SGB/SSA for doped samples suggest that grain boundaries are stabilized with respect to surfaces, thereby facilitating sintering and aggregation for grain boundary formation.

Surface segregation by EELS and EDS.

EELS and EDS combined with STEM revealed the expected enrichment of the dopants on the surface of TiO_2 nanocrystals. The techniques could not determine dopant segregation to grain boundaries due to the exceedingly small dimensions of the particles (5-10 nm) and the limits of the method. Figure 3 shows the STEM/EELS investigation for Ti050Ba.

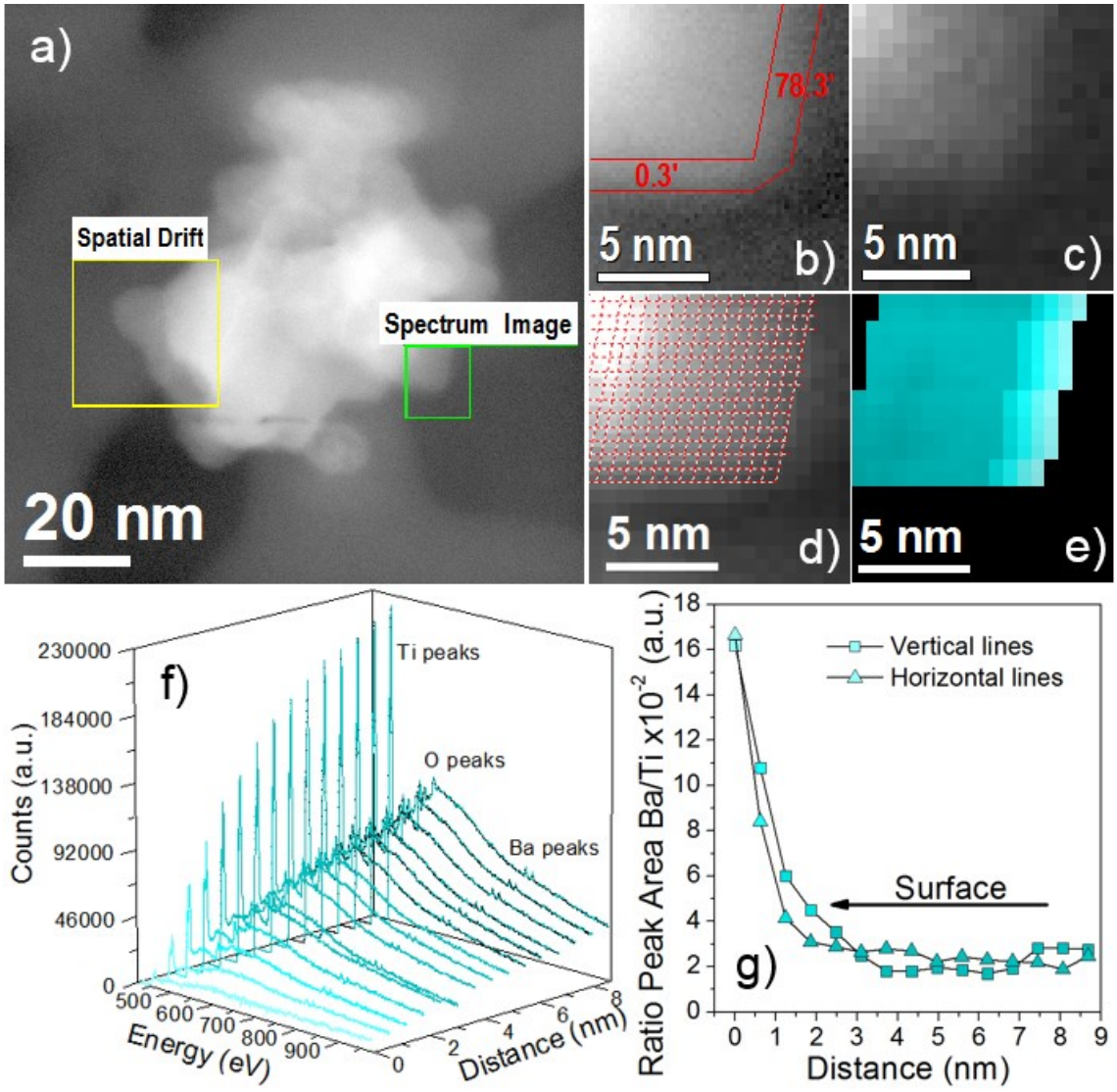

Figure 3. EELS measurement for a TiO_2 nanoparticle. a) Dark Field image of an aggregated BaO-doped TiO_2 nanoparticles. b) the area measured with 3x zoom. c) EELS spectrum image for the same area shown in Fig. 3b. d) line profiles used for EELS signal integration. e) EELS spectrum image with the extracted vertical array used for EELS signal integration. f) 3D plot EELS spectra integrated from each vertical line; with the Ti background removed, and g) the ratio area peaks between Ba and Ti for both horizontal and vertical integrated lines. Figures 3e,f,g were colored in blue corresponding to the Ba enrichment.

Figure 3a shows a dark field image of an agglomerate of particles. Figure 3b shows a zoomed image of the area of interest (indicated as 'spectrum imaging') with the lines marking the regions where the contrast is reduced for both edges. One edge makes an angle of 78.3 degrees with the horizontal axis, and the other edge makes an angle of 0.3 degrees. Because of the inconclusive EELS spectrum taken directly from the particle area, as shown in Figure 3c, we proposed to exploit the higher sensitivity of line scans to build a line scan grid representative of the particle composition profile. We used the angles that delineated the particles to generate the integrated EELS line profiles, as seen in Figure 3d. We called the line profile with the angle of 78.3 degrees the 'vertical line' and the line profile with the angle of 0.3 degrees the horizontal line.

Figure 3f shows a representative example of the multiple spectra taken along a line scan. Here, the intensities of the Ti L_2 and L_3 peaks are reduced, while the intensities of the Ba L_2 and L_3 peaks remain almost constant when moving from the interior of the grain (8 nm) to the surface (0 nm). The result indicates a Ba surface enrichment, as further evidenced in Figure 3g through the ratios between Ba and Ti peaks. Data collected for all lines were combined and plotted in Figure 3e, revealing a clear enrichment of Ba on a particular surface of the nanocrystal.

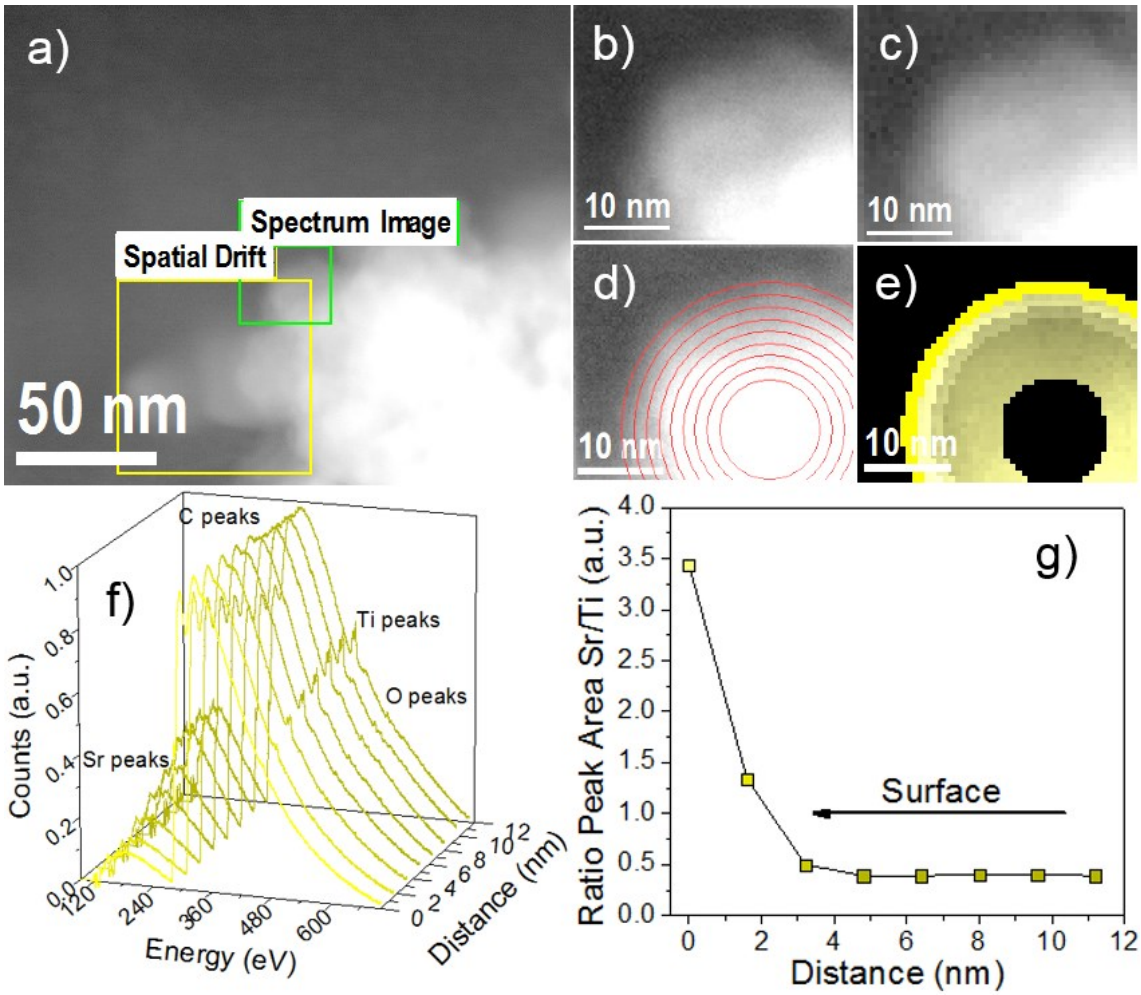

Figure 4. a) dark Field image of an aggregated TiO_2 nanoparticles doped with Sr. b) 3x zoom of the area measured (green box). c) EELS spectrum image of the same area shown in Figure 4b. d) circular rings area used for EELS signal integration. e) EELS spectrum image with the extracted rings array. f) 3D plot EELS spectra integrated from the circular area; with the Sr background removed, and g) the ratio area peaks between Sr and Ti. Figures 4e,f,g were colored in yellow corresponding to Sr enrichment.

Energy Electron Loss Spectroscopy (EELS) was also used to verify the Sr^{2+} surface segregation for Ti050Sr nanoparticles. Figure 4a shows the survey STEM image, with the study focusing on a particle located on the edge, as seen in Figure 4b. Figure 4c shows the respective EELS spectrum image for the particle, with an insufficient resolution to detail segregation of Sr^{2+} to the surfaces. Considering the isotropic particle shape, we used circular, linear scans centered in the middle of the particle, as shown in Figure 4d, to assess Sr^{2+} enrichment. The EELS spectra for different regions are shown in Figure 4f for the concentric lines closer to the surface (0 nm) and near the particle center (12 nm). The spectra generally show the presence of carbon, likely related to carbonate formation. The relationship between Sr and Ti signals is consistent with surface segregation. Figure 4g shows a value of around 0.5 for the Sr/Ti ratio in the

interior of the particle and 3.5 on the surface. Figure 4e compiles the Sr/Ti intensity ratio data and the location in the sample for better visualization of the Sr^{2+} enrichment.

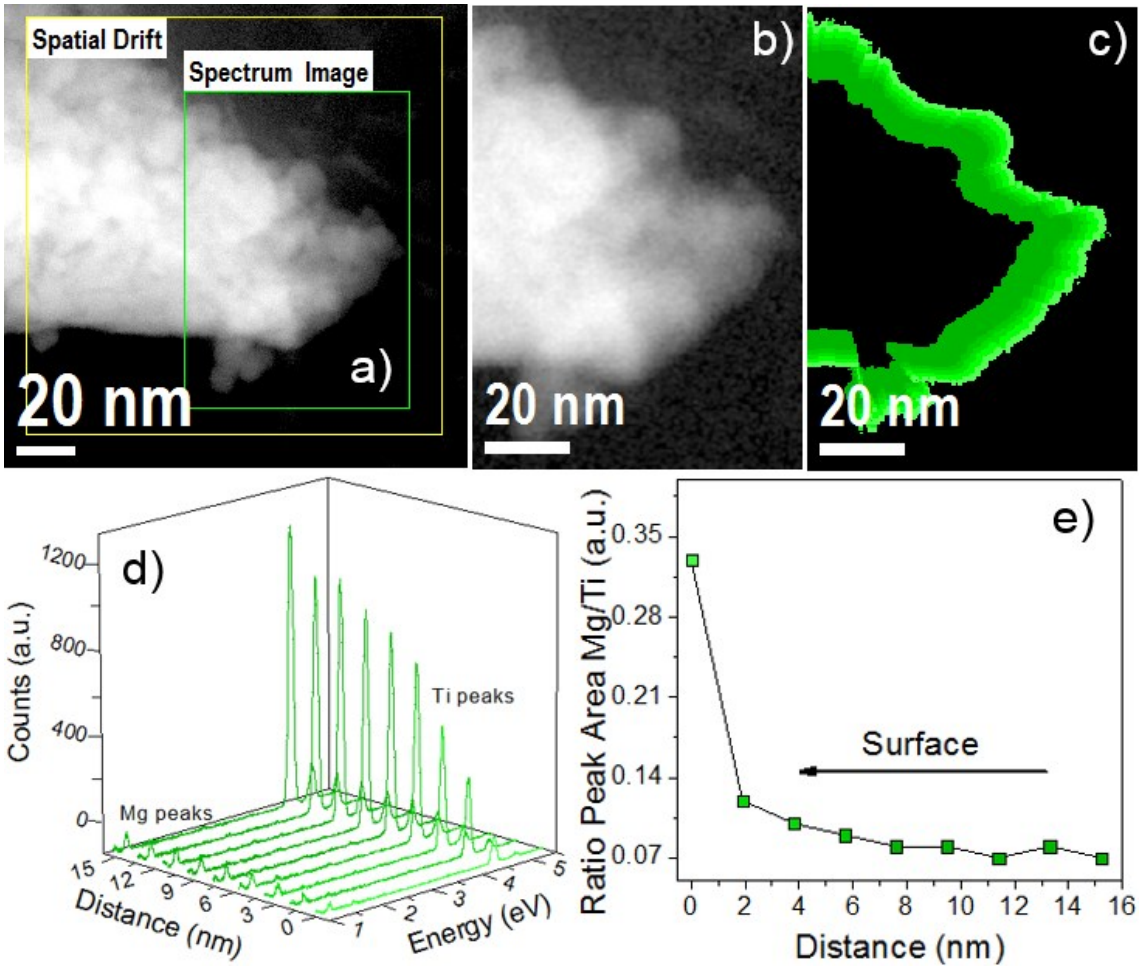

Figure 5. a) dark Field image of an aggregated TiO_2 nanoparticles doped with Mg. b) EDS spectrum image with 1.3x zoom of the area measured (green box). c) irregular masks area used for EDS signal integration. d) 3D plot EDS spectra integrated from irregular masks area, and e) the ratio area peaks between Mg and Ti. Figures 5c,d,e were colored in green corresponding to the enrichment of Mg.

A similar surface segregation analysis was performed for Mg-doped TiO_2 but using energy dispersive spectroscopy (EDS) instead. Figure 5a shows the survey image evidencing an agglomerate of nanoparticles. For the spectral image, we used the counter of the agglomerate shown in Figure 5b to integrate the signals related to Mg/Ti peaks (Figures 5c and 5d). The results suggest that consistent with the other dopants; the Mg content presents an enrichment on the surface of TiO_2 nanoparticles (Figure 5e).

Although Ca^{2+} was not tested for direct segregation through EELS or EDS, the data strongly suggest all alkaline earth metals have spontaneous segregation energies. Furthermore, when comparing the data from Figures 3, 4, and 5, one observes a direct

dependence of the segregation on the ionic radius. Ba^{2+}, Sr^{2+}, and Mg^{2+} showed enrichment of eight, seven, and five times on the TiO_2 surface, respectively.

Surface segregation by XPS.

XPS spectra also revealed dopant excess by elemental analysis on the surface of the nanoparticles. The complete X-ray photoelectron spectra for Ti050Mg, Ti050Ca, Ti050Sr, and Ti050Ba are shown in Figure S4. The study was performed in samples before and after the lixiviation process designed to remove soluble segregating elements from the surface. Table 4 compiles the atomic concentration (atom %) calculated from the spectra for samples before and after the lixiviation process. The supporting information also contains the selected element spectra for Ti 2p, O1s, and C1s (Figures S5, S6, and S7, respectively).

All compositions showed high oxygen, carbon, and titanium content on the surface. The spectrum component at 458.9 eV (Ti $2p_{3/2}$) is associated with the TiO_2 phase (Figure S5). The amount of titanium among the samples was similar, and no significant differences were observed. The peaks for the lixiviated samples generally presented a wider width (FWHM). This suggests a slight increment in the disorder of the TiO_2 structure on the surface. The oxygen (O 1s) spectra are shown in Figure S6. The main component of the oxygen spectra is associated with O-Ti bonds of the TiO_2, which is also observed a wider width (FWHM) on the lixiviated samples. The oxygen is also associated with –OH, O-C, and O-C=O.

In the Ti050CaLix sample, we observe an increase in hydroxyl groups (531.2 eV) (Figure S6d). The lower binding energy contributes to the low intensity of the phases MgO at 529.7 eV and CaO at 529.5 eV. The SrO has the same binding energy as the TiO_2 (530 eV). Figure S7 shows the C1s spectra. The main component at 285 eV is related to hydrocarbons (C-H). The oxygenated groups of alcohol and ether are shown at 286.5 and 288.7 eV, respectively.

Combined, the XPS data support the information that the dopants are segregated on the surface of the nanoparticles, and that the segregation amount decreases after the lixiviation procedure. However, it is not simple to estimate precisely how deep the XPS signal penetration is, which would be necessary for an unequivocal quantitative analysis. The quantity of magnesium on the surface was reduced from 1.4 to 0.7 atom % after the lixiviation process. The adjusted spectra for one component at 89 eV are shown

in Figures 6a and 6b for non-lixiviated and lixiviated samples, respectively. The amount of calcium was reduced from 1.2 to 0.5 atom %. Its spectra associated with the CaO phase adjusted to the component 347.4 eV are shown in Figures 6c and 6d for non-lixiviated and lixiviated powders, respectively. The wide width after the lixiviation is also associated with a structural disorder.[25] Following the same tendency, the amount of strontium from the surface was reduced from 1.4 to 0.9 atom % after the lixiviation. The spectra associated with the phase SrO adjusted to the component 133.0 eV are shown in Figures 6e and 6f. The remaining dopant element can be related to the concentration of the dopant in the GB or the bulk of the crystal (solid solution), which is not accessible to the acid lixiviation.

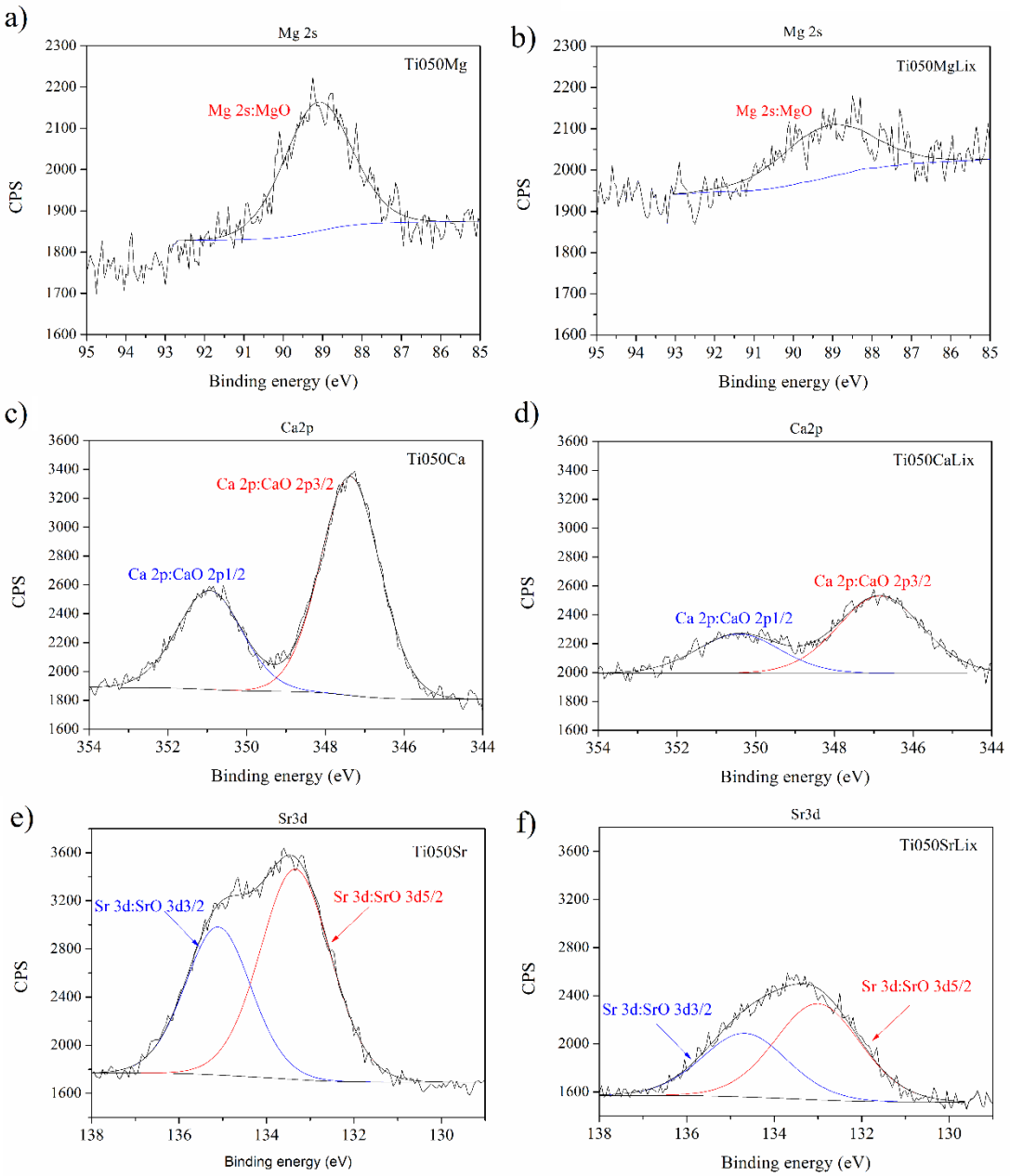

Figure 6. X-ray photoelectron spectra for Mg 2s, Ca 2p, and Sr 3d. (a) Ti050Mg, (c) Ti050Ca, and (e) Ti050Sr are non-lixiviated samples. (b) Ti050MgLix, (d) Ti050CaLix, and (f) Ti050SrLix are lixiviated samples.

Table 4. Atomic concentration (atom %) of the nanoparticles elements on the surface of doped TiO_2 samples before and after the lixiviation process obtained from ~~high resolution~~ the X-ray photoelectron spectra.

	Before lixiviation				**After lixiviation**			
Sample / element	Ti050Mg (% at.)	Ti050Ca (% at.)	Ti050Sr (% at.)	Ti050Ba (% at.)*	Ti050MgLix (% at.)	Ti050CaLix (% at.)	Ti050SrLix (% at.)	Ti050BaLix (% at.)*
Ti (Ti $2p_{3/2}$)	14.2	15.6	13.2	13.9	12.7	15.6	15.0	13.9
Dopant	1.4 (Mg 2s)	1.2 (Ca 2p)	1.4 (Sr 3d)	1.0 (Ba 3d)	0.7 (Mg 2s)	0.5 (Ca 2p)	0.9 (Sr 3d)	0.3 (Ba 3d)
Oxygen (O 1s)	46.8	48.7	42.7	43.3	42.9	48.0	47.5	42.5
Carbon (C1s)	37.6	34.5	42.7	41.8	44.2	35.0	36.6	43.3

* Data from the literature.[11]

Surface energies

Figure 7a shows the water adsorption isotherm for all the compositions studied. Figure 7b shows the measured heat of adsorption plotted against the water coverage, representing the total energy related to each dose adsorption shown in Figure 7a. Two stages are observed based on the derivative of the adsorption isotherm curve (Figure 7a). There is a rapid increase in coverage at very low relative pressures (<0.02) when the pressure increases. The enthalpies of water adsorption in this first stage are very negative, suggesting highly exothermic water reactions to the surface at the few monolayers. This is related to the dissociative nature of water due to the bond of chemisorbed water with the surface.[15,18] At the second stage, which is up to a relative pressure of about 0.4, the slope of the isotherm is lower, indicating the formation of multiple non-dissociated layers of water. At this point, the differential enthalpy of water adsorption gets close to the enthalpy of liquid water condensation, - 44 kJ/mol (dotted line in Figure 7b), which indicates that the new adsorbed layers show liquid-like behavior. Some of the curves show significant scattering at that point, which is an experimental issue linked to the formation of unstable layering of water molecules followed by local collapsing.[26,27]

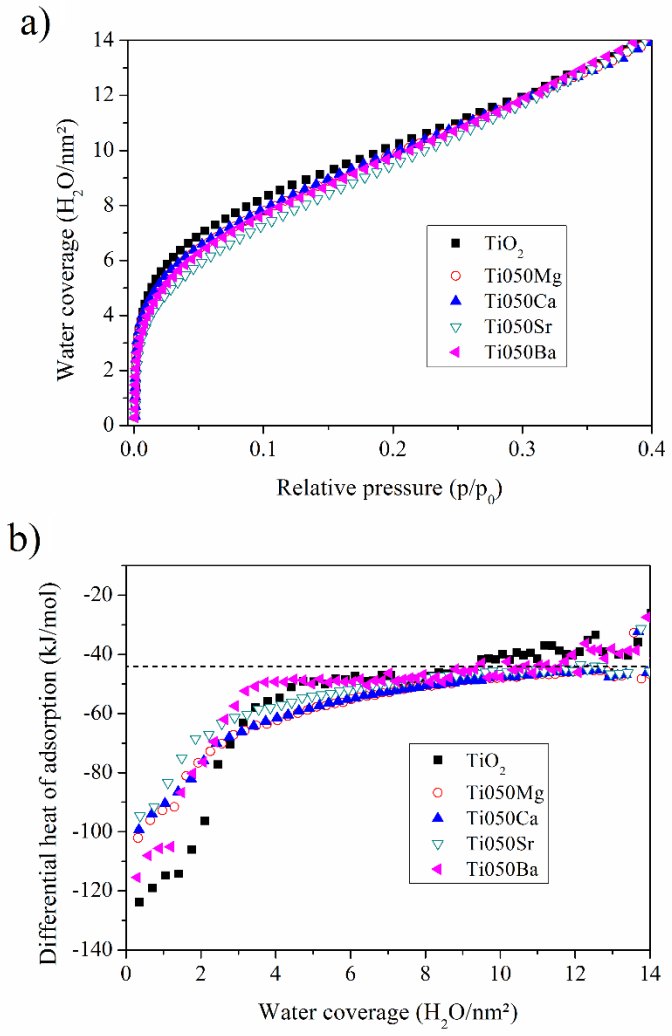

Figure 7. Water adsorption microcalorimetry data: water coverage isotherms plotted as H_2O molecules per nm² against the relative pressure (a), and enthalpy of water adsorption plotted against water coverage, (b).

We observe in Figure 7b that the undoped TiO_2 shows higher heats of adsorption as compared to the doped ones before leveling at -44 kJ/mol. This indicates that the dopants are systematically changing the surface chemistry, impacting the adsorption energies. Sr^{2+} shows the most impacting difference, reducing the reactivity of TiO_2 to H_2O by more than 100 kJ/mol at the first dose. This difference is surprising considering the hygroscopic nature of the dopants, but could be related to a higher affinity for CO_2 instead, as recently proposed.[12] The adsorption difference is better visualized by the integral of the adsorption curve shown in Figure S8. In integral form, a separation of the adsorption energies for the different samples is observed, which is proportional to the ionic radius. While this suggests increased stability of the surface by doping, we can use eq. 3 to calculate the surface energy of each compound.

The method exploits the thermodynamic relationship between the heat of water adsorption to the surface and the surface energy itself. The method relies on identifying the first point where the adsorption reaches the energy of liquefaction of water.[16] The integral allows better visualization of this point as the coverage where the curves converge to linearity. The point where this line tangents the experimental curve is identified as the splitting point, which can also be identified by the second derivative. Thus, the surface energy of the anhydrous surface was calculated by integrating the enthalpy of adsorption up to that coverage. Details of this method can be found elsewhere.[28]

Surface energies of undoped and alkaline earth metal doped TiO_2 as a function of ionic radius of dopant are shown in Figure 8. Since the surface energy of undoped TiO_2 is in the range of values found in the literature, one can assume that anhydrous anatase obeys the relationship described in eq. 3. The value found in this study can be compared to TiO_2 surface energies calculated by other methods, such as water adsorption (using the same setup, but different calculation methods as described in detail by Drazin 2014,[15] and reported by da Silva 2017,[18] and 2019[11]), high-temperature oxide melt solution of a series of samples of a given composition and structure but with distinct surface areas,[4] and computed surface energies calculation using density functional theory (DFT).[29] The dopants decreased the surface energy of TiO_2 nanoparticles, with Ba being the most effective dopant in doing so. The surface energy shows an almost linear decrease as a function of the ionic radius of the dopant. The slope of the curve changed for a higher ionic radius, suggesting a saturation point. The decrease in surface energy is associated with alkaline earth metal segregation together with CO_2 adsorption, which is spontaneous for TiO_2 and comes from the atmosphere, increasing with alkaline earth metal segregation.[12] Because it is not possible to separate both contributions, the influence of C or CO_x was not accounted for the nanostability of TiO_2 in this work.

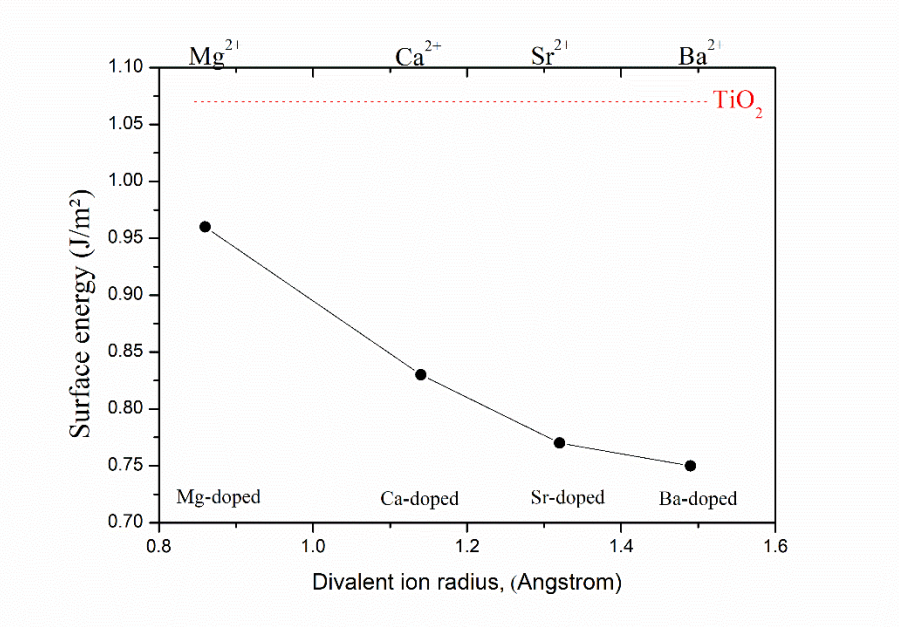

Figure 8. Surface energies of undoped and alkaline earth metals doped TiO_2 as a function of the divalent ion radius of the dopants. The surface energy of undoped TiO_2 is represented by the dotted red line.

Enthalpy of surface segregation.

The chemical analyses of the nanoparticles before and after the lixiviation process allowed the quantification of the interfacial excess (amount of segregated dopant) for all compositions (Table 5). The method exploited the solubility difference between the solute and the solvent in nitric acid. Segregated dopants could be removed from the surface of TiO_2 nanoparticles and then quantified using ICP. However, the lixiviation process only accesses the surface and not the grain boundary regions. To better understand the ion distribution in the system, one should compute segregation to both the surface and grain boundaries. The surface excess (Γ) can be calculated using eq. 6.

$$\Gamma = n_x/SSA \qquad (6)$$

where n_x is the number of moles of the lixiviated solute for each sample and SSA is the specific surface area (Table 3). The number of moles of each solute segregated in the grain boundary (n_{gb}) was calculated using the difference in total amount (n_T) of the solute, bulk solubility (n_{bulk}), and surface excess (n_s) as follows: $n_{gb} = n_T - n_{bulk} - n_s$. The large difference in the ionic radius, percent ionic character, electronegativity, and charge between the dopants and the solvent (bulk matrix) suggests that the solubility of the dopants in bulk is very low. Indeed, Hu *et al.*[30] determined that the solubility of BaO

in $BaTiO_3$ is lower than 100 ppm, which is negligible in our calculations. Consistent with this literature, for the calculations, we assumed solubility for all dopants to be 0.005 mol%.

The results are seen in Table 5. The surface and grain boundary excess increase systematically as the solute content increases. More pronounced segregation occurs in grain boundaries than to the surface. This is aligned with the relatively high grain boundary areas measured for all compositions (Table 3) — spontaneous formation of grain boundaries during synthesis results from moderately low grain boundary energies resulting from segregation. A similar phenomenon has been reported in Mn-doped SnO_2 and CeO_2 nanoparticles.[31,32]

The dopant distribution between the surface, the grain boundary segregation, and the bulk is driven by the total energy of the system.[11] During synthesis, the system has enough mobility to find the most stable energy state by balancing dopant segregation, interfacial areas, and solubility.[11,33] We applied the Langmuir-Mclean approach (eq. 7) to better understand the energetic dependences. The method was proposed by Chang *et al.*,[31] and states that segregation in the system should follow the equation:

$$\frac{x_j}{1-x_j} = \frac{x_B}{1-x_B}\exp\left(-\frac{\Delta H_j^{seg}}{RT}\right) \quad j = s \;\; or \;\; gb \tag{7}$$

where x_j is the fraction of segregated additive in the interface, x_B is the fraction of additive soluble in the bulk, and ΔH_j^{seg} is the heat of segregation.

Essentially, the distribution of dopants on the surface, grain boundaries, and bulk follows the conservation principle, and it can be written as eq. 8.

$$x_T = \sum_j f_j x_j = f_S x_S + f_{gb} x_{gb} + f_b x_b \tag{8}$$

here x_T and f_j are the total molar fractions of the solute and volume fractions, respectively. The volume fraction is calculated by eq. 9.

$$f_j = \sum_i \frac{V_j}{V_T} = \sum_i \rho m_j A_j \Omega^{1/3} \quad \text{where } \Omega = \frac{a.b.c}{nfu} \tag{9}$$

where a, b, and c are the lattice parameters, ρ is the density, A_j is the interface area, nfu is the number of TiO_2 per unit cell, and m_j is the number of monolayers. Based on the literature[11] and the data from the EELS/STEM analyzes, the number of monolayers was estimated as $m_s = 6$ and $m_{gb} = 6$. The surface and GB fractions x_S and x_{gb} can be calculated using eq. 10.

$$x_i = \frac{\Gamma_i A_i \mathrm{M}_w}{f_i} = \frac{\Gamma_i \mathrm{M}_W}{\rho \Omega^{1/3}} \quad \text{with } i = s \text{ or } gb \tag{10}$$

Combining eq. 7-10 and using the excess segregation data, the segregation energies were computed and are listed in Table 5. The values range from 27.8 to 36.7 kJ/mol, consistent with previously reported segregation energies.[11] The enthalpy of surface segregation increases proportionately to the ionic radius of the dopant, while the enthalpy of grain boundary segregation does not change significantly among the samples. For all dopants but Ba^{2+}, the grain boundary segregation energy is larger than the surface. That may be related to its large ionic radius, resulting in an increase in local strain at the grain boundary regions.

The spontaneous energy of segregation is deemed responsible for the observed microstructural evolution, with particle size reduction via doping. The ionic radius of the dopants plays an essential role in nanoparticle stabilization, which was shown by the lower surface energy and higher surface segregation enthalpy of the samples doped with dopants with a higher ionic radius. An interesting observation is the large segregation energies to the grain boundaries in all cases. This information is critical for a complete understanding of the nanoscale system and understanding doping in TiO_2 and other compositions.

Table 5. Surface excess, surface occupation of the dopant on the TiO_2 nanoparticle, grain boundary excess, interface fractions, and heats of segregation.

Sample	X mol% (dopant)	Γ (μmol/m²)	Surface occupation of the dopant on the TiO_2 nanoparticle (%)	Γ_{GB} (μmol/m²)	x_s	x_{gb}	$d\Delta H_s^{segr}(\frac{kJ}{mol})$		$d\Delta H_{gb}^{segr}(\frac{kJ}{mol})$	
MgO-doped TiO_2	0.00	0.00	0.00	0.00	0.0000	0.0000	0.0	$\Delta H_s^{segr} = -27.8 \pm 0.2$	0.0	$\Delta H_{gb}^{segr} = -36.1 \pm 2.6$
	0.10	0.04 ± 0.00	0.38	0.12 ± 0.00	0.0002	0.0009	−4.0		−7.2	
	0.73	0.48 ± 0.00	4.48	0.45 ± 0.01	0.0030	0.0058	−10.2		−11.9	
	5.23	1.87 ± 0.01	17.30	3.25 ± 0.08	0.0116	0.0445	−13.6		−17.1	
CaO-doped TiO_2	0	0.00	0.00	0.00	0.0000	0.0000	0.0	$d\Delta H_s^{segr} = -30.7 \pm 0.2$	0.0	$d\Delta H_{gb}^{segr} = -36.0 \pm 2.1$
	0.11	0.08 ± 0.00	0.99	0.11 ± 0.00	0.0007	0.0008	−6.5		−6.8	
	0.85	0.33 ± 0.00	4.01	0.64 ± 0.02	0.0028	0.0067	−10.4		−12.3	
	5.30	1.59 ± 0.01	19.53	2.40 ± 0.05	0.0142	0.0425	−14.1		−16.9	
SrO-doped TiO_2	0	0.00	0.00	0.00	0.0000	0.0000	0.0	$d\Delta H_s^{segr} = -33.1 \pm 1.4$	0.0	$d\Delta H_{gb}^{segr} = -36.6 \pm 4.4$
	0.12	0.03 ± 0.00	0.47	0.14 ± 0.00	0.0005	0.0009	−5.8		−7.3	
	1.05	0.33 ± 0.00	4.74	0.68 ± 0.02	0.0050	0.0068	−11.5		−12.3	
	6.46	1.55 ± 0.01	21.98	2.47 ± 0.08	0.0271	0.0451	−15.8		−17.1	
BaO-doped TiO_2	0.00	0.00	0.00	0.00	0.0000	0.0000	0.0	$d\Delta H_s^{segr} = -36.7 \pm 0.3$	0.0	$d\Delta H_{gb}^{segr} = -33.0 \pm 2.0$
	0.11	0.04 ± 0.00	0.63	0.11 ± 0.00	0.0009	0.0006	−7.2		−6.2	
	1.01	0.32 ± 0.00	5.19	0.63 ± 0.02	0.0077	0.0052	−12.6		−11.6	
	5.11	1.74 ± 0.01	27.91	1.80 ± 0.04	0.0421	0.0219	−16.9		−15.2	

Conclusions

TiO_2 nanoparticles doped with MgO, CaO, SrO, or BaO were synthesized using the polymeric precursor method, and the ions were confirmed to form a surface and grain boundary excess. TiO_2 anatase nanostability was improved due to ions segregation, which was quantified by a selective lixiviation method and qualitatively evidenced by EELS/EDS/STEM and XPS. The surface energies were measured by microcalorimetry and showed a decrease as a function of the dopant content. The effects of surface segregation on coarsening were confirmed by the reduction in crystallite sizes from ~17 to ~5 nm, which was even lower (~4 nm) for dopants with higher ionic radius, and the increase in specific surface area from ~45 to ~121 m^2/g for undoped TiO_2 and 5 mol% SrO-doped TiO_2, respectively. Enthalpies of segregation for all dopants on the surface and grain boundaries were first reported. The data are helpful to compute dopant distribution and microstructural evolution during synthesis, being a strategy for designing stable TiO_2-based photocatalysts.

Supporting Information

Simulated anatase XRD structure, crystallite domain size distribution, X-ray photoelectron spectra for Ti050Mg, Ti050Ca, and Ti050Sr samples, and integral heats of water adsorption.

- Author Information

Corresponding Author

*E-mail: andresilva.urussanga@gmail.com Tel.: +55 (11) 97414 5238

Notes

The authors declare no competing financial interest.

- Acknowledgments

We gratefully acknowledge support of the RCGI – Research Centre for Greenhouse Gas Innovation, hosted by the University of São Paulo (USP) and sponsored by FAPESP – São Paulo Research Foundation (2014/50279-4 and 2020/15230-5) and Shell Brasil, and the strategic importance of the support given by ANP (Brazil's National Oil, Natural

Gas and Biofuels Agency) through the R&D levy regulation. This research was also supported by LNNano – Brazilian Nanotechnology National Laboratory, CNPEM/MCTIC, TEM proposal n. 21831. RHRC thanks DMR Ceramics DMR 2015650.

- References

(1) Chen, X.; Selloni, A. Introduction: Titanium Dioxide (TiO 2) Nanomaterials. *Chem Rev* **2014**, *114* (19), 9281–9282. https://doi.org/10.1021/cr500422r.

(2) Chen, X.; Mao, S. S. Titanium Dioxide Nanomaterials: Synthesis, Properties, Modifications and Applications. *Chemical Reviews*. American Chemical Society 2007, pp 2891–2959. https://doi.org/10.1021/cr0500535.

(3) Hanaor, D. A. H.; Sorrell, C. C. Review of the Anatase to Rutile Phase Transformation. *J Mater Sci* **2011**, *46* (4), 855–874. https://doi.org/10.1007/s10853-010-5113-0.

(4) Levchenko, A. A.; Li, G.; Boerio-Goates, J.; Woodfield, B. F.; Navrotsky, A. TiO2 Stability Landscape: Polymorphism, Surface Energy, and Bound Water Energetics. *Chemistry of Materials* **2006**, *18* (26), 6324–6332. https://doi.org/10.1021/cm061183c.

(5) Castro, R. H. R.; Wang, B. The Hidden Effect of Interface Energies in the Polymorphic Stability of Nanocrystalline Titanium Dioxide. *Journal of the American Ceramic Society* **2011**, *94* (3), 918–924. https://doi.org/10.1111/j.1551-2916.2010.04164.x.

(6) da Silva, A. L.; Dondi, M.; Hotza, D. Self-Cleaning Ceramic Tiles Coated with Nb2O5-Doped-TiO2 Nanoparticles. *Ceram Int* **2017**, *43* (15), 11986–11991. https://doi.org/10.1016/J.CERAMINT.2017.06.049.

(7) da Silva, A. L.; Dondi, M.; Raimondo, M.; Hotza, D. Photocatalytic Ceramic Tiles: Challenges and Technological Solutions. *J Eur Ceram Soc* **2018**, *38* (4), 1002–1017. https://doi.org/10.1016/j.jeurceramsoc.2017.11.039.

(8) Andre, L.; Muche, D. N. F.; Dey, S.; Hotza, D.; Castro, R. H. R. Photocatalytic Nb 2 O 5 -Doped TiO 2 Nanoparticles for Glazed Ceramic Tiles. *Ceram Int* **2016**, *42* (4), 5113–5122. https://doi.org/10.1016/j.ceramint.2015.12.029.

(9) Miagava, J.; Da Silva, A. L.; Navrotsky, A.; Castro, R. H. R.; Gouvêa, D. The Nanocrystalline SnO2-TiO2System Part II: Surface Energies and

Thermodynamic Stability. *Journal of the American Ceramic Society*. 2016, pp 638–644. https://doi.org/10.1111/jace.13954.

(10) Nowotny, J. SURFACE AND GRAIN BOUNDARY SEGREGATION IN METAL OXIDES J. Nowotny Max-Planck-Institut FUr Festkorperforschung 7000 Stuttgart 80, F.R.G. **1989**, 205–239.

(11) da Silva, A. L.; Muche, D. N. F.; Caliman, L. B.; Bettini, J.; Castro, R. H. R.; Navrotsky, A.; Gouvêa, D. TiO 2 Surface Engineering to Improve Nanostability: The Role of Interface Segregation. *The Journal of Physical Chemistry C* **2019**, *123* (8), 4949–4960. https://doi.org/10.1021/acs.jpcc.8b12160.

(12) da Silva, A. L.; Wu, L.; Caliman, L. B.; Castro, R. H. R.; Navrotsky, A.; Gouvêa, D. Energetics of CO2and H2O Adsorption on Alkaline Earth Metal Doped TiO2. *Physical Chemistry Chemical Physics* **2020**, *22* (27), 15600–15607. https://doi.org/10.1039/d0cp01787f.

(13) Gandelman, H.; da Silva, A. L.; Caliman, L. B.; Gouvêa, D. Surface and Grain Boundary Excess of ZnO-Doped TiO2anatase Nanopowders. *Ceram Int* **2018**, *44* (10), 11390–11396. https://doi.org/10.1016/j.ceramint.2018.03.190.

(14) Gouvêa, D.; do Rosário, D. C. C.; Caliman, L. B. Surface and Grain-Boundary Excess of ZnO-Doped SnO2nanopowders by the Selective Lixiviation Method. *Journal of the American Ceramic Society* **2017**, *100* (9), 4331–4340. https://doi.org/10.1111/jace.14973.

(15) W. Drazin, J.; H. R. Castro, R. Water Adsorption Microcalorimetry Model: Deciphering Surface Energies and Water Chemical Potentials of Nanocrystalline Oxides. *The Journal of Physical Chemistry C* **2014**, *118* (19), 10131–10142. https://doi.org/10.1021/jp5016356.

(16) H. R. Castro, R.; V. Quach, D. Analysis of Anhydrous and Hydrated Surface Energies of Gamma-Al2O3 by Water Adsorption Microcalorimetry. *The Journal of Physical Chemistry C* **2012**, *116* (46), 24726–24733. https://doi.org/10.1021/jp309319j.

(17) Castro, R. H. R.; Benthem, K. van. *Sintering : Mechanisms of Convention Nanodensification and Field Assisted Processes*; Springer, 2013.

(18) da Silva, A. L.; Hotza, D.; Castro, R. H. R. Surface Energy Effects on the Stability of Anatase and Rutile Nanocrystals: A Predictive Diagram for Nb2O5-Doped-TiO2. *Appl Surf Sci* **2017**, *393*, 103–109. https://doi.org/10.1016/j.apsusc.2016.09.126.

(19) Zhang, H.; Ban, J. F.; Di, X. Structural Characteristics and Mechanical and Thermodynamic Properties of Nanocrystalline TiO2. *Chem Rev* **2014**, *114* (19), 9613–9644. https://doi.org/10.1021/cr500072j.

(20) Zhang, L. P.; Li, M.; Diebold, U. Characterization of Ca Impurity Segregation on the TiO2(110) Surface. *Surf Sci* **1998**, *412–413*, 242–251. https://doi.org/10.1016/S0039-6028(98)00432-4.

(21) Li, Y.; White, T. J.; Lim, S. H. Low-Temperature Synthesis and Microstructural Control of Titania Nano-Particles. *J Solid State Chem* **2004**, *177* (4–5), 1372–1381. https://doi.org/10.1016/J.JSSC.2003.11.016.

(22) Mi, J. L.; Clausen, C.; Bremholm, M.; Lock, N.; Jensen, K. M. A.; Christensen, M.; Iversen, B. B. Rapid Hydrothermal Preparation of Rutile TiO2 Nanoparticles by Simultaneous Transformation of Primary Brookite and Anatase: An in Situ Synchrotron PXRD Study. *Cryst Growth Des* **2012**, *12* (12), 6092–6097. https://doi.org/10.1021/cg301230w.

(23) Li, G.; Li, L.; Boerio-Goates, J.; Woodfield, B. F. High Purity Anatase TiO2 Nanocrystals: Near Room-Temperature Synthesis, Grain Growth Kinetics, and Surface Hydration Chemistry. *J Am Chem Soc* **2005**, *127* (24), 8659–8666. https://doi.org/10.1021/ja050517g.

(24) Zhang, H.; Chen, B.; Banfield, J. F. The Size Dependence of the Surface Free Energy of Titania Nanocrystals. *Physical Chemistry Chemical Physics* **2009**, *11* (14), 2553. https://doi.org/10.1039/b819623k.

(25) Haines, S. R.; Newton, A. W.; Weightman, P. Evaluation of the Surface Contribution to Disorder Broadened Core Level XPS Spectra in CuPd Alloys. *J Electron Spectros Relat Phenomena* **2004**, *137–140* (SPEC. ISS.), 429–434. https://doi.org/10.1016/j.elspec.2004.02.042.

(26) Pérez-Hernández, G.; Schmidt, B. Anisotropy of the Water-Carbon Interaction: Molecular Simulations of Water in Low-Diameter Carbon Nanotubes. *Physical Chemistry Chemical Physics* **2013**, *15* (14), 4995–5006. https://doi.org/10.1039/c3cp44278k.

(27) Yamada, T.; Tamamori, S.; Okuyama, H.; Aruga, T. Anisotropic Water Chain Growth on Cu(110) Observed with Scanning Tunneling Microscopy. *Phys Rev Lett* **2006**, *96* (3), 2–5. https://doi.org/10.1103/PhysRevLett.96.036105.

(28) Hasan, M. M.; Dey, S.; Nafsin, N.; Mardinly, J.; Dholabhai, P. P.; Uberuaga, B. P.; Castro, R. H. R. Improving the Thermodynamic Stability of Aluminate Spinel

Nanoparticles with Rare Earths. *Chemistry of Materials* **2016**, *28* (14), 5163–5171. https://doi.org/10.1021/acs.chemmater.6b02577.

(29) Hummer, D. R.; Kubicki, J. D.; Kent, P. R. C.; Post, J. E.; Heaney, P. J. Origin of Nanoscale Phase Stability Reversals in Titanium Oxide Polymorphs. *Journal of Physical Chemistry C* **2009**, *113* (11), 4240–4245. https://doi.org/10.1021/jp811332w.

(30) HU, Y. H.; HARMER, M. P.; SMYTH, D. M. Solubility of BaO in BaTiO3. *Journal of the American Ceramic Society* **1985**, *68* (7), 372–376. https://doi.org/10.1111/j.1151-2916.1985.tb10145.x.

(31) Chang, C.-H.; Gong, M.; Dey, S.; Liu, F.; Castro, R. H. R. Thermodynamic Stability of SnO 2 Nanoparticles: The Role of Interface Energies and Dopants. *The Journal of Physical Chemistry C* **2015**, *119* (11), 6389–6397. https://doi.org/10.1021/jp512969k.

(32) Wu, L.; Dey, S.; Gong, M.; Liu, F.; Castro, R. H. R. Surface Segregation on Manganese Doped Ceria Nanoparticles and Relationship with Nanostability. *The Journal of Physical Chemistry C* **2014**, *118* (51), 30187–30196. https://doi.org/10.1021/jp508663p.

(33) Gandelman, H.; da Silva, A. L.; Ramos, B.; Gouvêa, D. Interface Excess on Sb-Doped TiO2 Photocatalysts and Its Influence on Photocatalytic Activity. *Ceram Int* **2021**, *47* (1), 619–625. https://doi.org/10.1016/j.ceramint.2020.08.169.